Enhanced bulk conductivity of A-site divalent acceptor-doped non-stoichiometric sodium bismuth titanate

Fan Yang, Patrick Wu, Derek C. Sinclair *

Department of Materials Science and Engineering, University of Sheffield, S1 3JD, UK

ARTICLE INFO

ABSTRACT

Bismuth-deficient sodium bismuth titanate (nominally $Na_{0.5}Bi_{0.49}TiO_{2.985}$, $NB_{0.49}T$) is a good oxide-ion conductor. Here we report the influence of A-site divalent ions, $M^{2+} = Ca^{2+}$, Sr^{2+} and Ba^{2+}, on the electrical properties of $NB_{0.49}T$. A-site divalent doping for Bi^{3+} enhances the bulk (grain) conductivity by ~ one order of magnitude without changing the conduction mechanism, which is attributed to an increase in the oxygen vacancy concentration based on the doping mechanism $Bi^{3+} + \frac{1}{2} O^{2-} \rightarrow M^{2+}$. Among these three dopants, Sr^{2+} is the most effective in increasing the bulk conductivity due to a combination of its smaller mismatch in ion size with Bi^{3+}, its intermediate polarisability and lower bond strength to oxygen compared to Ca^{2+} and Ba^{2+}. Doping strategies for further improvements to bulk conductivity of NBT materials are discussed based on these results. Comparison with other oxide-ion conductors and initial stability test under reducing atmosphere show the doped non-stoichiometric NBT materials are promising for low and intermediate temperature applications.

1. Introduction

Oxide-ion conductors are widely used in various important technological devices such as solid oxide fuel cells (SOFCs), oxygen sensors, oxygen pumps, oxygen separation membranes, etc. [1–4]. In the past decade, there has been rapid progress on the research of oxide-ion conductors, driven by the requirements for new clean energy sources, sensors and so on [5].

Recently, a new family of oxide-ion conductors based on the ferroelectric perovskite sodium bismuth titanate ($Na_{0.5}Bi_{0.5}TiO_3$, NBT) was reported [6,7]. High ionic conductivity was found in bismuth-deficient NBT, i.e., $Na_{0.5}Bi_{0.49}TiO_{2.985}$, $NB_{0.49}T$, which originates from oxygen vacancies generated according to the following Kroger-Vink equation

$$2Bi_{Bi}^{x} + 3O_{O}^{x} \rightarrow 2V_{Bi}''' + 3V_{O}^{\bullet\bullet} + Bi_2O_3. \tag{1}$$

Furthermore, the highly polarisable Bi^{3+} ions with their $6s^2$ lone-pair electrons and weak Bi—O bonds provide pathways with low diffusion barriers [6,8–10], which is beneficial for the migration of oxygen ions. The predominant oxide-ion conduction in $NB_{0.49}T$ has been confirmed by electromotive force (EMF) measurements, which show an ionic transport number $t_i > 0.9$ at 600–700 °C [6]. The calculations in Ref. [8–10] reveal the lowest migration barriers for oxygen vacancies occur in saddle points between two A-sites and a Ti-site when both A-sites are Bi ions, whereas higher barriers are observed for A-site

combinations of Na and Bi or 2 Na ions. The values vary with the distribution of the rest of the A-site sublattice. Experimentally, there is no evidence for long range order of the A-site cations in NBT and therefore the Bi-Na-Ti saddles points are considered to be the rate limiting step in the overall oxygen ion migration in undoped NBT.

Further enhancement of ionic conductivity was achieved by doping Mg^{2+} onto the Ti-site of $NB_{0.49}T$, which generated more oxygen vacancies according to

$$MgO + Ti_{Ti}^{x} + O_{O}^{x} \rightarrow Mg_{Ti}'' + V_{O}^{\bullet\bullet} + TiO_2. \tag{2}$$
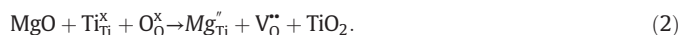
2% Mg-doped $NB_{0.49}T$ (nominally $Na_{0.5}Bi_{0.49}Ti_{0.98}Mg_{0.02}O_{2.965}$) ceramics achieved a bulk ionic conductivity comparable to that of Gd-doped CeO_2 at temperatures <400 °C [6].

The calculations performed in Ref. [9] have led to the suggestion that the ionic conductivity of NBT-based materials could be further improved by introducing suitable dopants on the A-site. The computational results showed that although acceptor-type B-site dopants such as Mg^{2+} for Ti^{4+} create oxygen vacancies they also significantly increase the oxygen migration barriers by binding with oxygen vacancies and therefore A-site acceptor doping is more promising to achieve high conductivity. For example, Na or K doped NBT, $Na_{0.5}(Bi_{0.46}Na_{0.04})TiO_{2.96}$ and $Na_{0.5}(Bi_{0.46}K_{0.04})TiO_{2.96}$, according to the calculations can induce higher bulk conductivity than Mg-doped NBT at the same oxygen vacancy concentration. The enhancement of conductivity is attributed to the fact that the disordered A-site sublattice can form different local atomistic configurations to accommodate the electrostatic and strain fields of the dopants. The first principle calculations do provide guidance to the

---

* Corresponding author.
  E-mail address: d.c.sinclair@sheffield.ac.uk (D.C. Sinclair).

potential experimental doping strategies for NBT to enhance the oxide-ion conductivity; however, the A-site non stoichiometry in undoped NBT has been shown experimentally [6,7] to be substantially below the compositions that was simulated in Ref. [9].

Here, divalent ions from the group IIA family, specifically Ca^{2+}, Sr^{2+} and Ba^{2+}, were doped on the A-site by partial 1:1 replacement for Bi^{3+} ions and their effect on the bulk electrical conductivity was investigated. The results are discussed from the perspective of the concentration and mobility of the charge carriers. The purpose of this study is not only to explore Ca^{2+}, Sr^{2+} and Ba^{2+} as doping ions for NBT from the IIA family but also to find dopant selection criteria and doping strategies to obtain yet higher bulk conductivity in NBT-based materials.

2. Experimental

Powders with nominal starting compositions of $Na_{0.5}Bi_{0.49}TiO_{2.985}$ and $Na_{0.5}Bi_{0.47}M_{0.02}O_{2.975}$ (M = Ca, Sr and Ba) were prepared by the solid-state reaction method using Na_2CO_3 (99.5%, Fisher chemical, UK), Bi_2O_3 (99.9%, Acros Organics, USA), TiO_2 (99.9%, Sigma Aldrich, UK), $CaCO_3$ (99.0%, Sigma Aldrich, UK), $SrCO_3$ (99.9%, Sigma Aldrich, UK) and $BaCO_3$ (99.0%, Sigma Aldrich, UK) as starting materials. Prior to weighing, the raw powders were dried overnight at 300 °C for Bi_2O_3 and Na_2CO_3, 180 °C for the other carbonates and 800 °C for TiO_2. Appropriate amounts of each precursor were weighed and mixed thoroughly in isopropanol using yttria-stabilised zirconia grinding media for 6 h. The mixture was dried at 85 °C overnight, sieved and then calcined for 2 h at 800 °C. The resultant powders were subjected to a second round of ball milling, drying, sieving and calcination, and finalised by a third round of ball milling and sieving. The final products were compacted into pellets by uni-axial cold pressing using poly vinyl alcohol (PVA) as binder. Pellets were embedded in sacrificial powder of the same composition and sintered at 1150 °C for 2 h after evaporating the binder at 550 °C for 2 h.

The density of sintered pellets was measured by the Archimedes' method. Phase purity was identified by X-ray diffraction on the crushed pellets using a high resolution STOE STADI-P diffractometer (STOE & Cie GmbH, Darmstadt, Germany) operating with $CuK_{\alpha 1}$ radiation with a linear position sensitive detector. The crushed pellets were annealed at 400 °C for 4 h to eliminate any residual stress caused by crushing and grinding. Lattice parameters were determined by structural refinement for reflections in the range of $10° \leq 2\theta \leq 100°$ using EXPGUI [11,12]. Ceramic microstructure was observed by scanning electron microscopy on thermally-etched surfaces using a JEOL JSM-6010LA (JEOL LTd., Tokyo, Japan) SEM. Grain compositions were obtained by energy dispersive X-ray spectroscopy (EDS) on polished samples (without thermal etch).

Electrical properties of the pellets were obtained from ac impedance spectroscopy using an Agilent E4980A impedance analyser (Agilent Technologies Inc., Palo-Alto, CA) and/or a Solarton 1260 system (Solartron Analytical, UK). Before measurements, Au or Pt paste was coated on the polished surfaces of the samples and fired at 800 or 900 °C for 2 h to serve as electrodes. Impedance data were collected from 150 to 600 °C with an interval of 25 °C during both heating and cooling. The equilibrium time between measurements was 25 min. Impedance measurements were also carried out in N_2, air and O_2 using Pt electrodes. All impedance data were corrected for the high frequency inductance by performing a short circuit measurement and normalised by a geometric factor (thickness/surface area). Equivalent circuit fitting was performed using ZView software (Scribner Associates, Inc., Southern Pines, NC). Oxygen-ion transport number measurements were performed using a Probostat system (NorECs Norwegian Electro Ceramics AS, Oslo, Norway). A sample was sealed onto an YSZ tube using a commercial glass frit. An oxygen partial pressure (pO_2) difference was created across the ceramic by flowing N_2 into the YSZ tube and leaving the outside of the ceramic in air. The pO_2 difference was monitored by measuring the voltage across the inner and outer electrodes on the YSZ tube. The voltage was measured using a Keithley 182 sensitive digital voltmeter.

3. Results

3.1. XRD, SEM

XRD patterns show all samples are phase pure (Fig.1). Their structure could be refined to a rhombohedral cell (space group $R3c$). The
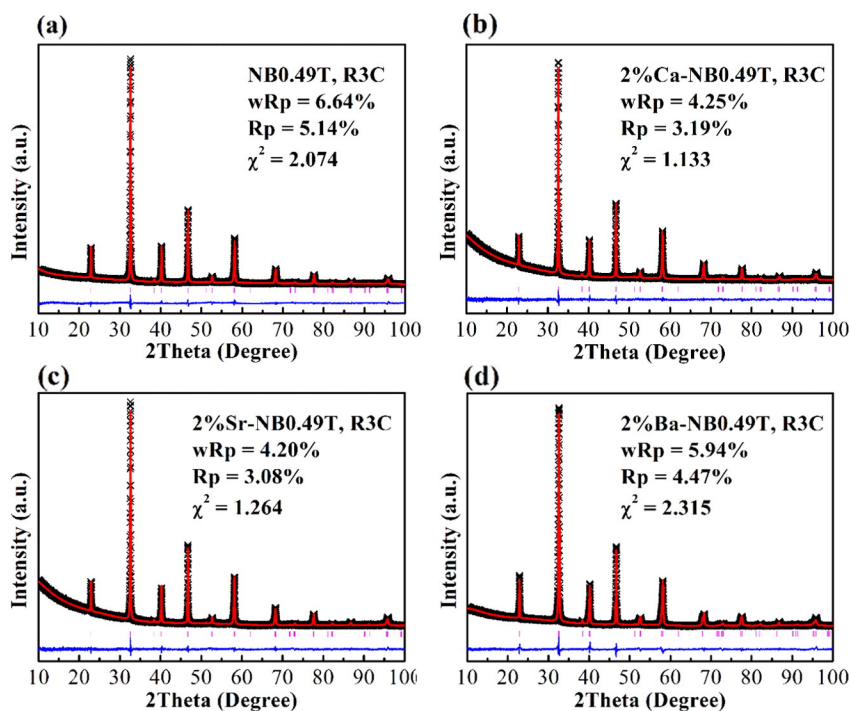

Fig. 1. Rietveld refinement of the room temperature XRD pattern of (a) $NB_{0.49}T$, (b) 2%Ca-doped $NB_{0.49}T$, (c) 2%Sr-doped $NB_{0.49}T$ and (d) 2%Ba-doped $NB_{0.49}T$. The cross symbols represent the observed pattern and the solid line shows the calculated fit. The reflection marker for the $R3c$ structure is shown as vertical lines with the difference pattern below the diffraction pattern. The quality of fit is indicated in each figure.

Table 1
Lattice parameters, density (theoretical X-ray, measured and relative) and average grain size of $NB_{0.49}T$, 2%Ca, 2%Sr and 2%Ba-doped $NB_{0.49}T$ ceramics.

|	Lattice parameters			Density			Average grain size (μm)
	a (Å)	c (Å)	V (Å³)	ρ_{th} (g/cm³)	ρ (g/cm³)	Relative (%)	
$NB_{0.49}T$	5.4932	13.4963	352.70	5.926	5.65	95.3	7.2
2%Ca-doped $NB_{0.49}T$	5.4918	13.4926	352.42	5.836	5.66	97.0	3.5
2%Sr-doped $NB_{0.49}T$	5.4923	13.4965	352.59	5.860	5.61	95.7	3.0
2%Ba-doped $NB_{0.49}T$	5.4924	13.5384	353.69	5.869	5.62	95.8	8.1

lattice parameters obtained from Rietveld refinement are listed in Table 1. The 2%Ba-doped $NB_{0.49}T$ has a larger cell volume than the other three due to the larger ion size of Ba^{2+} (1.61 Å, XII coordinated [13]) than Ca^{2+} (1.34 Å [13]), Sr^{2+} (1.44 Å [13]) and Bi^{3+} (~1.39 Å). The ionic size of Bi^{3+} in XII-coordination is not available. The value for Na^+, 1.39 Å, is used as $r(Bi^{3+})$ due to the fact that the mismatch between Na^+ and Bi^{3+} is close to zero in NBT [14]. Pellet density was >95% of their theoretical values. SEM images of the thermally-etched surfaces show larger grains of undoped and Ba-doped $NB_{0.49}T$ than Ca, Sr-doped $NB_{0.49}T$ (Fig.2). The average grain sizes are also listed in Table 1.

Although XRD patterns suggest these ceramics are phase pure, SEM on polished surfaces show the presence of secondary phase (Fig.3). EDS analysis on these secondary phase particles indicates they are rich in Na and Ti, with a Na:Ti ≈ 1:3. It's possible that the secondary phase is $Na_2Ti_6O_{13}$. Chemical compositions of the main phase of these ceramics are listed in Table 2. For undoped $NB_{0.49}T$ and 2%M-doped $NB_{0.49}T$, the theoretical Bi/Na ratio is 0.98 and 0.94, respectively. The EDS results give values of 0.97 for $NB_{0.49}T$ and ~0.95 for 2%M-doped $NB_{0.49}T$, respectively. The M^{2+} concentration is close to its nominal level. The Ti percentage in all samples (~49.0%) is slightly lower but within 2 or 3 standard deviations of the theoretical value (50.0%).

3.2. Impedance spectroscopy

A typical complex impedance plane plot of these ceramics shows three arcs (Fig. 4a). From high to low frequency (left to right), they represent the response from the grains (bulk), grain boundaries and electrode effects, respectively. An equivalent circuit of three resistor-constant phase elements (R-CPE) connected in series (inset figure) was used to fit the data. The impedance residuals, defined as $Z_{residual} = (Z_{measured} - Z_{fitted})/|Z_{measured}|$, are used to present the difference between the measured and fitted data. The impedance residuals are <2% within the frequency range (Fig.4b), indicating the validity of the selected equivalent circuit and giving confidence in the extracted resistance values. The impedance spectra of other samples show similar features. To avoid unnecessary duplication, they are not presented here.

Bulk conductivity values, σ, were calculated from the reciprocal of the resistance, and plotted in an Arrhenius format (Fig. 5a). The σ-1/T relationship of undoped $NB_{0.49}T$ shows two regions; temperatures below ~320 °C with a higher activation energy (region 1) and temperatures above ~320 °C with a lower activation energy (region 2). The switching temperature is associated with the maximum in permittivity observed in dielectric spectroscopy measurements; however, the
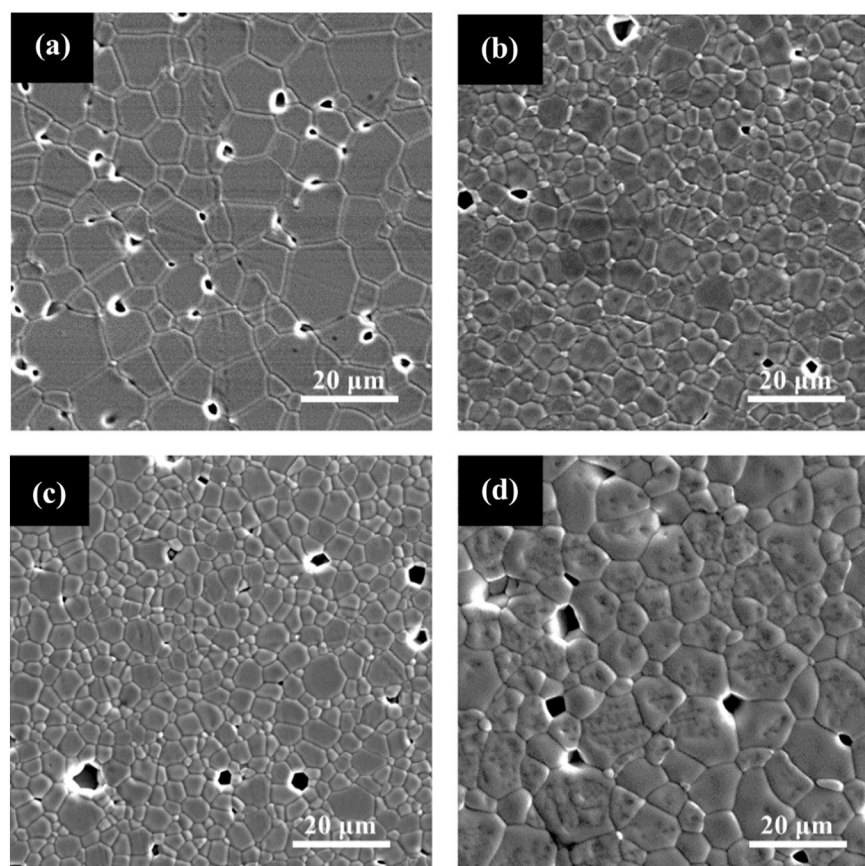
Fig. 2. SEM micrographs of thermally-etched surfaces of (a) $NB_{0.49}T$, (b) 2%Ca-doped $NB_{0.49}T$, (c) 2%Sr-doped $NB_{0.49}T$ and (d) 2%Ba-doped $NB_{0.49}T$.
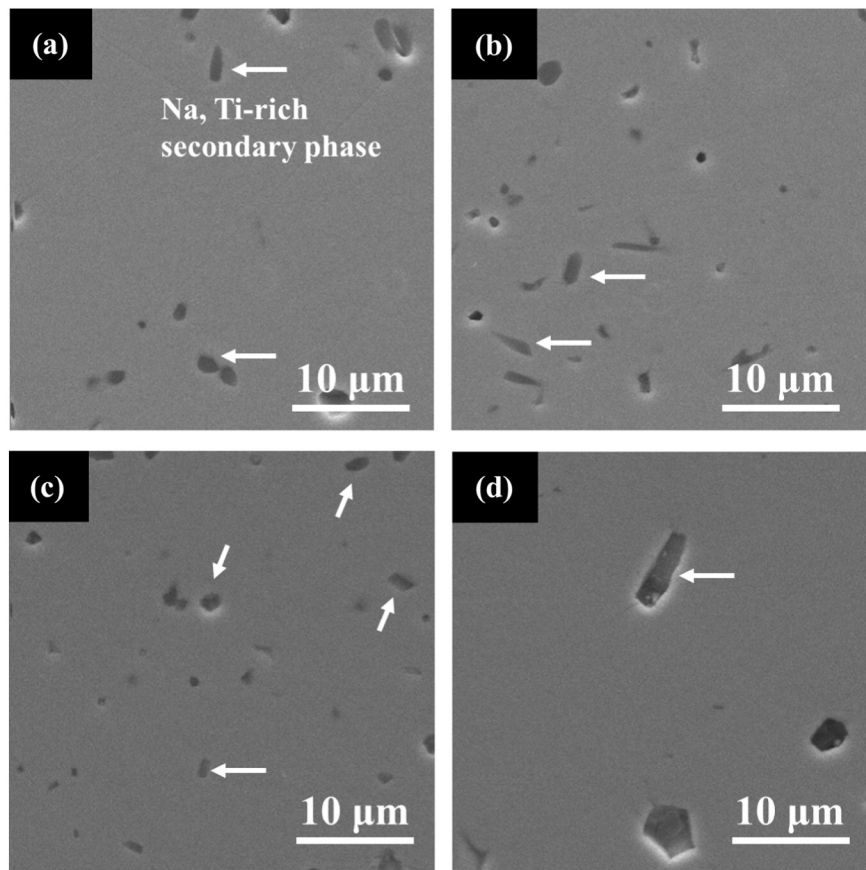
Fig. 3. SEM micrographs of polished surfaces (without thermal-etch) of (a) $NB_{0.49}T$, (b) 2%Ca-doped $NB_{0.49}T$, (c) 2%Sr-doped $NB_{0.49}T$ and (d) 2%Ba-doped $NB_{0.49}T$. The arrows indicate some secondary phase grains.

reason(s) for a change of activation energy around this temperature remain(s) unclear. The doped samples show similar features but present higher conductivities than the undoped sample. A maximum enhancement of bulk conductivity of ~ one order of magnitude is observed for Sr-doped $NB_{0.49}T$ in the low temperature region and more than half order of magnitude in the high temperature region. Bulk conductivities at selected temperatures and associated activation energies in the two regions are given in Table 3 for comparison. Although M^{2+} doping increases the bulk conductivity, it also increases the activation energy.

Impedance measurements were also carried out in flowing nitrogen, air and oxygen atmospheres. The bulk conductivity is independent of the oxygen partial pressure (pO_2), as shown in Fig.5b using 2%Sr-doped $NB_{0.49}T$ as an example. The pO_2-independent conductivity suggests the electrical conduction is predominantly ionic over the limited T-pO_2 range investigated. The oxide-ion conduction mechanism is further confirmed by electromotive force measurement using N_2/air, which shows an ionic transport number to be ~0.95 at 600–700 °C.

3.3. Stability in 5%H_2/95%N_2

XRD patterns of 2%Sr-doped $NB_{0.49}T$ annealed in 5%H_2/95%N_2 at various temperatures for 12 h are shown in Fig. 6a. An additional peak for Bi metal could be detected after annealing at ≥600 °C, indicating that decomposition of the material was occurring. No additional reflection(s) were observed in XRD patterns for samples annealed at ≤550 °C. Furthermore, impedance measurements were carried out on the pellet annealed at 550 °C in H_2. The M″-log$f$ plot (measured at 200 °C) is identical to that before annealing (Fig.6b), which supports the evidence from XRD that 2%Sr-doped $NB_{0.49}T$ can be chemically stable and withstand 550 °C in 5% H_2.
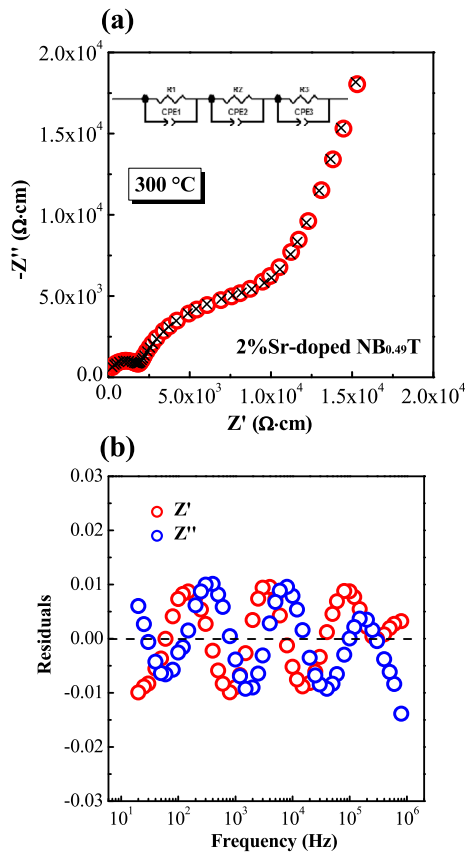
4. Discussion

4.1. Factors that influence bulk conductivity

4.1.1. Oxygen vacancy concentration

To achieve high oxide-ion conductivity the material should have a significant concentration of oxygen vacancies to facilitate charge carriers, as well as high oxygen ion mobility. When a divalent ion M^{2+} is introduced to replace Bi^{3+} in $NB_{0.49}T$, oxygen vacancies are formed according to the following Kroger-Vink equation

$$2MO + 2Bi_{Bi}^{x} + O_O^{x} \rightarrow 2M'_{Bi} + Bi_2O_3 + V_O^{\bullet\bullet}. \tag{3}$$

Occurrence of the above reaction is confirmed by the significant change of the maximum permittivity ($\varepsilon_{r\text{-max}}$) of $NB_{0.49}T$ after doping (Fig.7). The bulk permittivity was calculated from equivalent circuit fitting parameters based on the high frequency bulk response with $\varepsilon_r = R^{(1-n)/n}Q^{1/n}/\varepsilon_0$ [15], where ε_0 is the vacuum permittivity

Table 2
Analysed composition of the main phase of $NB_{0.49}T$, 2%Ca, 2%Sr and 2%Ba-doped $NB_{0.49}T$ ceramics determined by EDS. Data were collected from 10 randomly selected areas on polished surfaces (without thermal etch).

Starting composition	Na (at.%)	Bi (at.%)	M (at.%)	Ti (at.%)
$NB_{0.49}T$	25.9 ($\pm$0.2)	25.1 ($\pm$0.3)	N/A	49.0 ($\pm$0.2)
2%Ca-doped $NB_{0.49}T$	25.4 ($\pm$0.2)	24.5 ($\pm$0.5)	1.0 ($\pm$0.2)	49.1 ($\pm$0.4)
2%Sr-doped $NB_{0.49}T$	25.6 ($\pm$0.3)	24.3 ($\pm$0.3)	1.1 ($\pm$0.3)	49.0 ($\pm$0.3)
2%Ba-doped $NB_{0.49}T$	25.2 ($\pm$0.4)	24.2 ($\pm$0.5)	1.3 ($\pm$0.1)	49.3 ($\pm$0.3)

Fig. 4. Impedance spectroscopy and equivalent circuit fitting for a 2%Sr-doped $NB_{0.49}T$ ceramic measured at 300 °C in air. (a) Complex impedance (Z^*) plot. The inset figure is the equivalent circuit used to model the data. The open circles are the experimental data and the crosses are the fitting results; (b) impedance residuals showing the quality of fit.

8.85×10^{-14} F/cm. The significant increase in ε_{r-max} for the large and polarisable Ba^{2+} ions in 2% Ba-doped $NB_{0.49}T$ and the significant decrease in ε_{r-max} for the smaller and less polarisable Ca^{2+} in 2% Ca-doped $NB_{0.49}T$, together with the shift of the temperature at which the permittivity shows its maximum, T_m, give evidence that the dopants are incorporated into the host lattice.

The bulk conductivity of several NBT materials is plotted against oxygen vacancy concentration in Fig. 8. The oxygen vacancy concentration for $NB_{0.50}T$, $NB_{0.49}T$ and M^{2+}-doped $NB_{0.49}T$ was calculated from the nominal chemical formula of each composition as doping or deliberately induced Bi_2O_3 deficiency is believed to be the major source of oxygen vacancies. Furthermore, EDS analysis of $NB_{0.49}T$ and M^{2+}-doped $NB_{0.49}T$ confirmed the analysed composition to be in agreement with the nominal starting composition, Table 2. Therefore, the oxygen vacancy concentration calculated from nominal compositions is adequate for the purpose of ranking. It's clear that M^{2+}-doping increases the oxygen vacancy concentration and thus enhances the bulk conductivity.

4.1.2. Ionic size of the dopant

At a fixed oxygen vacancy concentration, conductivity shows dependence on the ionic size of the dopant, as also revealed by Fig. 8. The conductivity plotted against the ratio of the dopant ionic radius $r(M^{2+})$ to the host ionic radius $r(Bi^{3+})$ is shown in Fig.9. The highest conductivity is observed for Sr-doped $NB_{0.49}T$ with $r(Sr^{2+})/r(Bi^{3+})$ ~ 1.05. Such an optimum r_{dopant}/r_{host} value of 1.05 is also observed in other perovskite such as $LaAlO_3$ [16–18] and $LaGaO_3$ [19–21]. Under the optimum r_{dopant}/r_{host}, there is minimum elastic strain in the host crystal lattice, which is believed to be beneficial for the migration of charge carriers [22].

From a structural view point, ionic conductivity of perovskite-type oxides is often dependent on the tolerance factor, t, and specific free volume, V_{sf}. t is determined by the ionic radii of the various ions as $t = (r_A + r_O)/\sqrt{2}(r_B + r_O)$, where r_A, r_B are the mean ionic radii for A and B site cations and r_O is the ionic radius of oxygen ion. A small t represents large lattice distortion and thus is detrimental to ionic conduction [23]. The specific free volume is defined as $V_{sf} = (V - \sum V_{ion})/V$ [22], where V is the unit cell volume and can be calculated using an empirical equation $V = [2.37r_B + 2.47 - 2.00(s-1)]^3$ [24], where s is the reciprocal of t. A large V_{sf} provides larger channels for oxygen ions to move and thus beneficial for ionic conduction. Hayashi et al. summarised electrical conductivity data from the literature and found an optimum t of ~0.96 to obtain maximum conductivity in perovskites with low oxygen deficiency due to the balance between V_{sf} and t [22]. In this work, the doping level is too low to have a noticeable influence on t and V_{sf}, as shown in Table 4. The contribution from any structural parameter to the enhanced conductivity can therefore be excluded.

4.1.3. Doping site

First principle calculation results suggest that doping site is important to the enhancement of conductivity of NBT. B-site doping increases the diffusion barrier by binding with oxygen vacancies and therefore decreases the mobility of charge carriers [9]. Here we compare the conductivity of A-site M^{2+}-doped $NB_{0.49}T$ with B-site Mg^{2+}-doped $NB_{0.49}T$, as shown in Fig.8. At the same doping level, e.g., 2%, substitution of Ti^{4+} by Mg^{2+} at the B-site results in a higher oxygen vacancy concentration than the substitution of Bi^{3+} by Ca^{2+}, Sr^{2+} or Ba^{2+} at the A-site; however, the conductivity does not show much improvement. This is consistent with the first-principle calculation results that B-site doping may not be the most desirable mechanism for increasing the conductivity of NBT
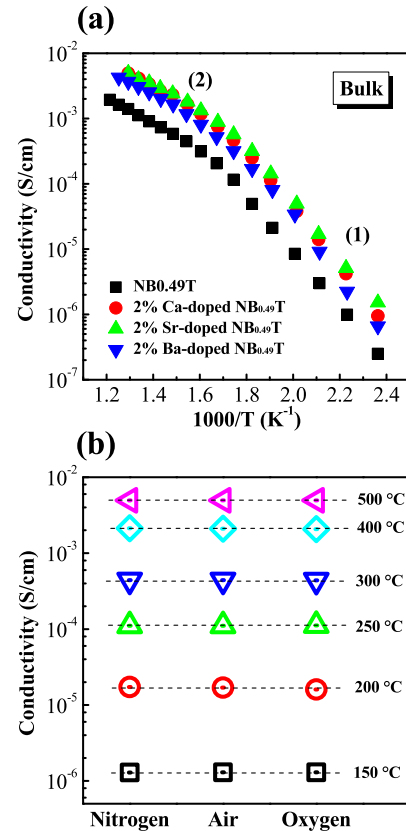
Fig. 5. (a) Arrhenius plot of bulk conductivity of $NB_{0.49}T$, 2%Ca-doped, 2%Sr-doped and 2%Ba-doped $NB_{0.49}T$ ceramics; (b) bulk conductivity of 2%Sr-doped $NB_{0.49}T$ ceramic measured in air, nitrogen and oxygen at selected temperatures.

Table 3
Bulk conductivity at selected temperatures and the associated activation energy values for $NB_{0.49}T$, 2%Ca, 2%Sr and 2%Ba-doped $NB_{0.49}T$ ceramics.

	σ (S/cm)				Ea (eV)	
	200 °C	300 °C	400 °C	500 °C	(1)	(2)
$NB_{0.49}T$	2.99×10^{-6}	1.16×10^{-4}	5.85×10^{-4}	1.40×10^{-3}	0.85 ± 0.01	0.41 ± 0.01
2%Ca-doped $NB_{0.49}T$	1.41×10^{-5}	4.64×10^{-4}	2.31×10^{-3}	4.92×10^{-3}	0.91 ± 0.01	0.53 ± 0.02
2%Sr-doped $NB_{0.49}T$	1.69×10^{-5}	5.72×10^{-4}	2.42×10^{-3}	4.95×10^{-3}	0.87 ± 0.02	0.48 ± 0.01
2%Ba-doped $NB_{0.49}T$	9.18×10^{-6}	3.18×10^{-4}	1.65×10^{-3}	3.66×10^{-3}	0.95 ± 0.03	0.43 ± 0.01

materials as it increases the diffusion barrier by binding with oxygen vacancies which decreases the mobility of charge carriers. However, it's not possible to make a concrete conclusion that A-site is superior to B-site doping based on the current experimental results. First, the actual Mg-doping level in the Mg-doped $NB_{0.49}T$ ($Na_{0.5}Bi_{0.49}Ti_{0.98}Mg_{0.02}O_{2.965}$) is not clear. EDS analysis reveals the Mg content in the bulk phase is only half of its nominal value [6]. This suggests either the Mg-doping level is <2 at.% or is related to the proximity of Kα lines for Na (1.04 keV) and Mg (1.25 keV). Second, the ionic size mismatch between Mg^{2+} and Ti^{4+} is large ($r(Mg^{2+})/r(Ti^{4+}) \sim 1.19$). It's possible that doping a smaller ion, e.g., Ga^{3+}, will result in a higher conductivity.

4.1.4. Polarisability and bonding strength with oxygen of the dopants

It's accepted that the highly polarisable Bi^{3+} ions and weak Bi—O bonds in NBT are critical to achieve high mobility of oxygen ions as ionic conduction occurs by a hopping mechanism through the saddle point (i.e., a triangle defined between two A-site ions and a B-site ion) in perovskites [6,8–10]. Therefore, apart from ionic size, the polarisability and bonding strength with oxygen should also be considered when selecting dopants for A-site substitution. As listed in Table 5, among

the three dopants chosen for study here, Ba^{2+} has the highest polarisability, however, it also has the highest bonding strength with oxygen. The competing effect from these two parameters, along with the large ionic size mismatch with Bi^{3+}, limits the ionic conductivity enhancement in Ba-doped $NB_{0.49}T$. Sr^{2+} has intermediate polarisability and the lowest bonding strength with oxygen for the group IIA ions under consideration as A-site acceptor dopants, as well as a smaller ion size mismatch with Bi^{3+}, which makes it the most effective of these dopants. High bonding strength between dopant and oxygen ions decreases the mobility of oxygen vacancies by associating with oxygen vacancies to form defect clusters, as well as blocking ion conduction pathways. This explains why M^{2+}-doped $NB_{0.49}T$ ceramics have higher bulk activation energies for conduction compared to undoped $NB_{0.49}T$.

In summary, the bulk ionic conductivity of $NB_{0.49}T$ can be improved by doping M^{2+} ions to substitute Bi^{3+}. The enhanced conductivity is mainly attributed to the increased oxygen vacancy concentration. To achieve high conductivity, the dopant ion should not only have an optimum size mismatch with Bi^{3+} but also have a large polarisability and a low bonding strength with oxygen to maintain high mobility of the charge carriers. Among the three group IIA dopants chosen, Sr^{2+} shows the best performance. However, we propose that with increasing doping level, the effect from an increase in the oxygen vacancy concentration will be offset by low polarisability and high bonding strength with oxygen as compared to Bi^{3+}, thus limiting further significant improvement in the bulk ionic conductivity. In addition, we predict the partial replacement of the highly polarisable Bi^{3+} ion with its low bonding strength to oxygen by isovalent doping of La^{3+} with a similar ionic radius but much lower polarisability and much higher bond strength, see Table 5, will dramatically decrease the oxide-ion conductivity in NBT.

4.2. Comparison with other oxide-ion conductors

The bulk conductivity of $NB_{0.49}T$ and Sr-doped $NB_{0.49}T$ is compared with several best known oxide-ion conductors in Fig. 10. At low
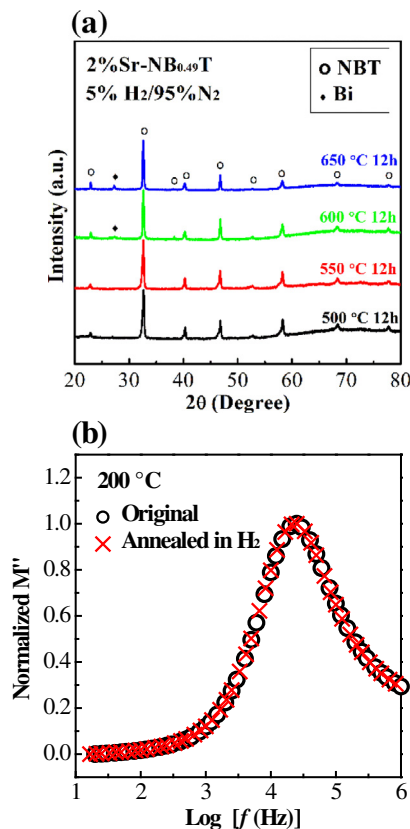
Fig. 6. (a) XRD patterns of 2%Sr-doped $NB_{0.49}T$ pellets after annealing in 5% H_2/N_2 at various temperatures for 12 h; (b) M″-log$f$ plots at 200 °C for 2%Sr-doped $NB_{0.49}T$ before (open circle) and after annealing (cross) in 5% H_2/N_2 at 550 °C for 12 h.
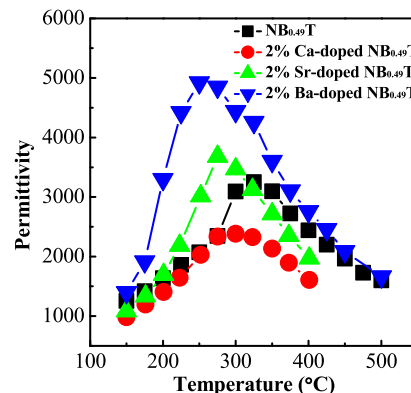
Fig. 7. Permittivity of $NB_{0.49}T$ and Ca, Sr, Ba-doped $NB_{0.49}T$ as a function of temperature.
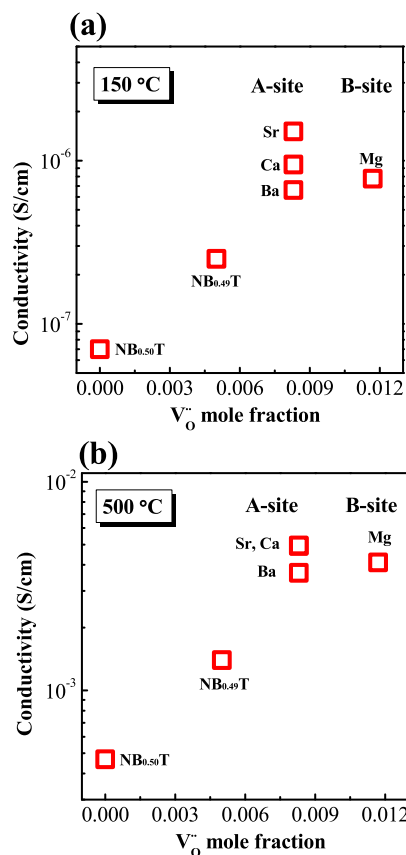
Fig. 8. Relationship between bulk conductivity and oxygen vacancy concentration at (a) 150 and (b) 500 °C. The values NB$_{0.50}$T and Mg-doped NB$_{0.49}$T are extracted from Ref. [6] for comparison.

Fig. 9. Dependence of bulk ionic conductivity on the dopant to host ionic radius ratio in M^{2+}-doped NB$_{0.49}$T at (a) 150 and (b) 500 °C.

temperatures (<300 °C), Sr-doped NB$_{0.49}$T shows a bulk conductivity ~2 orders of magnitude higher than (BiO$_{1.5}$)$_{0.8}$(ErO$_{1.5}$)$_{0.2}$, 20ESB and ~one order of magnitude higher than (BiO$_{1.5}$)$_{0.88}$(DyO$_{1.5}$)$_{0.08}$(WO$_3$)$_{0.04}$, 8D4WSB. At higher temperatures, i.e., 500 °C, the conductivity of Sr-doped NB$_{0.49}$T is still comparable to Ce$_{0.9}$Gd$_{0.1}$O$_{1.95}$, 10GDC and 20ESB. It also shows negligible degradation with time [31] on the contrary to the rapid degradation of bulk ionic conductivity of 20ESB and 8D4WSB [32,33]. Furthermore, it has an advantage over stabilised δ-Bi$_2$O$_3$ oxide-ion conductors as a more sustainable (rare-earth element free) material for low and intermediate temperature applications.

5. Conclusion

Partial replacement (2 at.%) of Bi^{3+} with Ca^{2+}, Sr^{2+} or Ba^{2+} on the A-site of NB$_{0.49}$T improves the bulk conductivity up to ~one order of magnitude without changing the conduction mechanism. The enhanced conductivity is mainly due to an increase in the oxygen vacancy concentration. Among the three dopants, Sr^{2+} is the most effective in increasing the bulk conductivity and this is attributed to its optimum ionic size mismatch with the host Bi^{3+} ions, its relatively high polarisability and reasonable bonding strength with oxygen ions. However, we cast doubt on further significant enhancements of the ionic conductivity by increasing M^{2+} doping levels by partial replacement of Bi^{3+} ions because the gain from an increase in the oxygen vacancy concentration will be off-set by the lower polarisability and high bonding strength of the M^{2+} ions with oxygen. On the other hand, the conductivity enhancement may also be restricted by the low solid solution limits of dopants. Initial results with higher doping levels show additional XRD peaks from a Na, Ti-rich secondary phase for doping levels ≥4%. Further
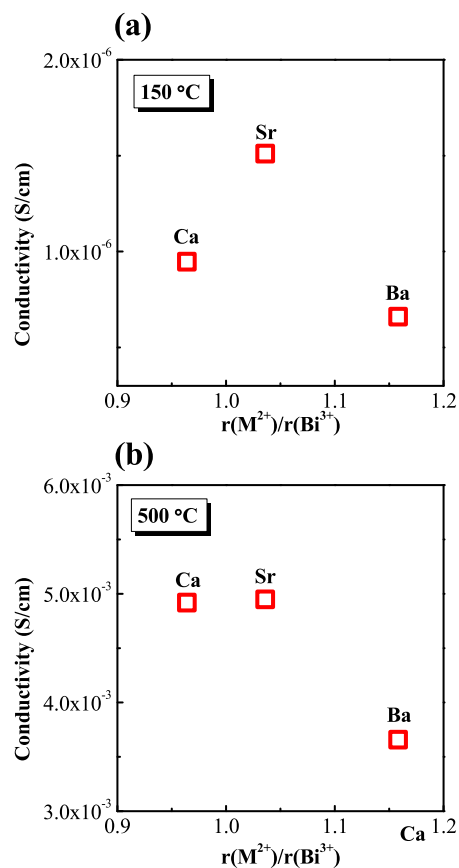
experimental work is being carried out in attempts to verify this suggestion and will be reported in detail elsewhere.

Compared with other 'best known' oxide-ion conductors, Sr-doped NB$_{0.49}$T shows superior ionic conductivity below 300 °C and insignificant degradation in the intermediate-temperature range. Initial results show Sr-doped NB$_{0.49}$T is stable under a reducing atmosphere of 5% H$_2$/95% N$_2$ up to 550 °C. Although the long-term stability under reducing atmosphere is yet to be investigated, the initial results show that if decomposition does occur it's not immediate and therefore presumably NB$_{0.49}$T–based materials could be used as part of a bi-layer electrolyte, e.g., using gadolinia-doped ceria (GDC) as a buffer layer [34]. Therefore, NB$_{0.49}$T-based oxide-ion conductors are promising for low and intermediate temperature applications. Further work is in progress to achieve higher conductivity via chemical doping and to understand the local structure-conductivity relationship(s) in NBT materials.
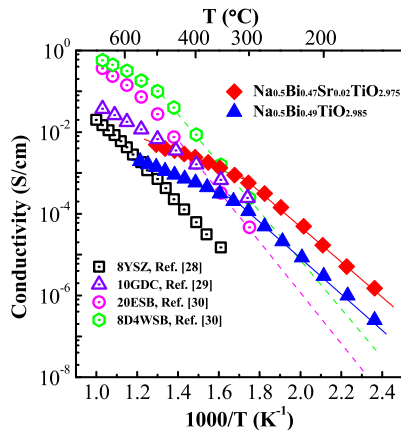
Acknowledgement

Table 4
Tolerance factor and specific free volume for NB$_{0.49}$T, 2%Ca, 2%Sr and 2%Ba-doped NB$_{0.49}$T ceramics.

Composition	Tolerance factor	Specific free volume
NB$_{0.49}$T	0.9792	0.1949
2%Ca-doped NB$_{0.49}$T	0.9788	0.1967
2%Sr-doped NB$_{0.49}$T	0.9796	0.1970
2%Ba-doped NB$_{0.49}$T	0.9808	0.1968

Table 5
Ionic radius, polarisability and bonding strength with oxygen of several possible A-site dopant ions. Data for polarisability (except La^{3+}) and bonding strength with oxygen are from Ref. [25,26], respectively.

Dopant	Ionic radius (XII-coordination, [Å])	Polarisability [$Å^3$]	Bonding strength with oxygen [kJ·mol^{-1}]
Na^+	1.39	1.80	257
K^+	1.64	3.83	239
Ca^{2+}	1.34	3.16	464
Sr^{2+}	1.44	4.24	454
Ba^{2+}	1.61	6.40	563
Bi^{3+}	1.39	6.12	343
La^{3+}	1.36	4.82 [27]	799

Fig. 10. Bulk conductivity of $NB_{0.49}T$ and Sr-doped $NB_{0.49}T$ in comparison with $Zr_{0.852}Y_{0.148}O_{1.926}$, 8YSZ [28], $Ce_{0.9}Gd_{0.1}O_{1.95}$, 10GDC [29], $(BiO_{1.5})_{0.8}(ErO_{1.5})_{0.2}$, 20ESB [30] and $(BiO_{1.5})_{0.88}(DyO_{1.5})_{0.08}(WO_3)_{0.04}$, 8D4WSB [30].

References

[1] T. Hibino, A. Hashimoto, T. Inoue, J. Tokuno, S. Yoshida, M. Sano, Science 288 (2000) 2031.
[2] B.C.H. Steele, Mater. Sci. Eng. B13 (1992) 79–87.
[3] W.C. Maskell, Solid State Ionics 134 (2000) 43–50.
[4] A.Q. Pham, R.S. Glass, Electrochim. Acta 43 (1998) 2699–2708.
[5] S.J. Skinner, J.A. Kilner, Materials Today 6 (2003) 30–37.
[6] M. Li, M.J. Pietrowski, R.A. De Souza, H. Zhang, I.M. Reaney, S.N. Cook, J.A. Kilner, D.C. Sinclair, Nat. Mater. 13 (2014) 31–35.
[7] M. Li, H. Zhang, S.N. Cook, L. Li, J.A. Kilner, I.M. Reaney, D.C. Sinclair, Chem. Mater. 27 (2015) 629–634.
[8] J.A. Dawson, H. Chen, I. Tanaka, J. Mater. Chem. A 3 (2015) 16574–16582.
[9] X. He, Y. Mo, Phys. Chem. Chem. Phys. 17 (2015) 18035–18044.
[10] M.S. Islam, J. Mater. Chem. 10 (2000) 1027–1038.
[11] A.C. Larson, R.B. Von Dreele, "General Structure Analysis System (GSAS)", Los Alamos National Laboratory Report LAUR, 1994 86–748.
[12] B.H. Toby, J. Appl. Crystallogr. 34 (2001) 210–213.
[13] R.D. Shannon, Acta Crystallographica Section A 32 (1976) 751–767.
[14] G.O. Jones, P.A. Thomas, Acta Crystallographica Section B 58 (2002) 168–178.
[15] J. Fleig, Solid State Ionics 150 (2002) 181–193.
[16] J.A. Kilner, P. Barrow, J. Brook, J. Power Sources 3 (1978) 67–80.
[17] H. Iwahara, Solid State Ionics 52 (1992) 99–104.
[18] K. Nomura, S. Tanase, Solid State Ionics 98 (1997) 229–236.
[19] T. Ishihara, H. Matsuda, Y. Takita, J. Am. Chem. Soc. 116 (1994) 3801–3803.
[20] T. Ishihara, H. Matsuda, M.A. Bustam, Y. Takita, Solid State Ionics 86-88 (1996) 197–201.
[21] P. Huang, A. Petric, J. Electrochem. Soc. 143 (1996) 1644–1648.
[22] H. Hayashi, H. Inaba, M. Matsuyama, N.G. Lan, M. Dokiya, H. Tagawa, Solid State Ionics 122 (1999) 1–15.
[23] J. Ranløv, N. Bonanos, F.W. Poulsen, M. Mogensen, Solid State Phenom. 39-40 (1994) 219–222.
[24] O. Fukunaga, T. Fujita, J. Solid State Chem. 8 (1973) 331–338.
[25] N.M. Grimes, R.W. Grimes, J. Phys. Condens. Matter 10 (1998) 3029–3034.
[26] Y.R. Luo, Comprehensive Handbook of Chemical Bond Energies, CRC Press, Boca Raton, FL, 2007.
[27] C. Vineis, P.K. Davies, T. Negas, S. Bell, Mater. Res. Bull. 31 (1996) 431–437.
[28] Y. Arachi, H. Sakai, O. Yamamoto, Y. Takeda, N. Imanishai, Solid State Ionics 121 (1999) 133–139.
[29] T. Zhang, P. Hing, H. Huang, J. Kilner, Solid State Ionics 148 (2002) 567–573.
[30] D.W. Jung, K.L. Duncan, E.D. Wachsman, Acta Mater. 58 (2010) 355–363.
[31] F. Yang, H. Zhang, L. Li, I.M. Reaney, D.C. Sinclair, Chem. Mater. 28 (2016) 5269–5273.
[32] S.H. Jung, E.D. Wachsman, N. Jiang, Ionics 8 (2002) 210–214.
[33] N. Jiang, E.D. Wachsman, J. Am. Ceram. Soc. 82 (1999) 3057–3064.
[34] E.D. Wachsman, K.T. Lee, Science 334 (2011) 935–939.